Imaging Cargo Containers Using Gravity Gradiometry

Barry Kirkendall, Yaoguo Li, and Douglas Oldenburg

***Abstract*—Identifying fissile materials inside cargo shipping containers is a current national security need. We propose using the geophysical technique of gravity gradiometry to image cargo shipping containers for the purpose of detecting high-density materials. We focus on developing the necessary numerical algorithms and carrying out feasibility studies without being concerned with engineering, instrumentation, and application issues. To obtain realistic images with sharp boundaries, robust estimators are applied to the model objective function of the inversion operator and coupled with a Huber norm to provide stable numerical computation. We explicitly form the linear and nonlinear resolution matrices to quantify the resolution errors and perform a funnel analysis to quantify the variance of the recovered densities. Assuming a realistic data acquisition pattern requiring a reasonable amount of time, we show that it is possible to identify high-density materials with a minimum volume of 15 cm^3. Finally, we provide a recovered density threshold to suggest the presence of high-density materials from an arbitrary recovered density model and apply this to two examples of recovering concealed fissile material from a cargo container.**

***Index Terms*—Density image, gravity measurement, inverse problems, optimization methods, robustness.**

I. Introduction

ALTHOUGH the technique of gravity gradiometry [1] is close to 100 years old, applications have dramatically increased partly due to recent advances in electronics and microprocessors. Such applications include airborne-based remote sensing [2], [3], basin analysis [4], marine geophysical surveys [5], mining geophysics [6], and borehole geophysics [7]. These applications rely on the large density contrast of geologic targets and the improved accuracy of modern gravity gradiometers for sensing the gradients of gravity fields. Because of the density variation of cargo contents, the same technology should also be applicable to imaging the cargo containers. The application of gravity gradiometry applied to imaging cargo inside metallic shipping containers has clear advantages over other traditional remote-sensing techniques but has not been studied in scientific literature. The impetus for this paper is the current domestic and international need to develop rapid noninvasive imaging techniques to detect fissile material and export-controlled items within cargo shipping containers.

The metallic cargo-container shell is constructed from a derivative of carbon steel, which precludes the use of electric and magnetic techniques due to the high electrical conductivity, magnetic susceptibility, and variable wall thickness. Low-frequency electromagnetic time- and frequency-domain fields can penetrate the container shell and remain focused, but the usable frequency must be below 300 Hz [8], which does not allow sufficient electromagnetic induction or resolution. Seismic techniques are also not applicable as the items inside a cargo container have poor mechanical coupling with the container. Neutron and gamma imaging have been widely studied, but they generate radiation that could be problematic in the presence of biological material or sensitive integrated circuits [9]. The high density of fissile materials in contrast to common commercial goods suggests that precise measurement of the gravity field that is produced by the cargo contents may provide an alternative inspection technique. For example, plutonium, a fissile material, has a density of 19 g/cm^3, whereas the densities of water and aluminum are 1 and 2 g/cm^3, respectively. Detection of these density contrasts can be made with either traditional gravimeters or gravity gradiometers. The former measures the vertical component of the gravity field, and the latter one senses the spatial gradient of gravitational acceleration that is produced by mass distribution. Modern gravity gradiometers typically measure with identical pairs of accelerometers rotating at a constant angular velocity [6] but can also measure by precisely quantifying the deflection, or scissoring, of orthogonal bars that are mounted inside a cryogenic container.

We propose an inspection technique (Fig. 1) using gravity gradiometry to identify the presence of fissile materials in cargo containers and conduct numerical simulations to ascertain the feasibility of the proposed technique. Since this is a feasibility study focusing on theoretical and numerical aspects, issues that are connected with the development of a prototype are left for future research. Our method first reconstructs a 3-D density distribution within a synthetic cargo container by performing a generalized inversion of gravity-gradient data that are measured from an array of gradiometry sensors as a cargo container is passed between them. The total mass within the cargo container, configuration of mass distribution, and lower and upper bounds of identified high-density regions are then examined to infer the possible presence of fissile materials. In this paper, we will review the gravity-gradiometry technique,

Manuscript received April 21, 2006; revised October 6, 2006. This work was supported in part by the Lawrence Livermore National Laboratory Advanced Study Program.

B. Kirkendall is with the Colorado School of Mines, Golden, CO 80401 USA, and also with Lawrence Livermore National Laboratory, Livermore, CA 94550 USA (e-mail: Kirkendall1@llnl.gov).

Y. Li is with the Department of Geophysics, Colorado School of Mines, Golden, CO 80401 USA (e-mail: ygli@mines.edu).

D. Oldenburg is with the Department of Earth and Ocean Sciences, University of British Columbia, Vancouver, BC V6T 1Z4, Canada (e-mail: doug@eos.ubc.ca).

Color versions of one or more of the figures in this paper are available online at http://ieeexplore.ieee.org.

Digital Object Identifier 10.1109/TGRS.2007.895427

0196-2892/$25.00 © 2007 IEEE

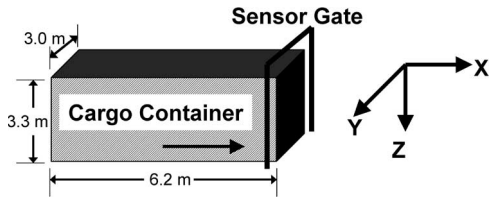

Fig. 1. Illustration of the proposed technique and axis coordinates. The cargo container is passed through a gate of sensors on the top and on both sides. Stationary sensors decrease noise levels to 1 eötvös. In practice, this manner of acquisition can provide extremely dense data coverage, although this paper will assume lower density coverage in intervals of 0.3 m. These intervals are seen as the dotted black lines over the discretized model space in Fig. 2.

the inversion algorithm and associated techniques developed and implemented by the authors that are used in constructing 3-D density distributions, and methods that are developed to estimate the resolution and uncertainty of the inverted density distribution. A synthetic example is shown to illustrate the feasibility of the proposed technique.

II. Gravity-Gradiometry Technique

The technique of gravity gradiometry [10] is based on multiple point measurements of the gravity field and calculation of the local gradient from those data. Several advantages from specifically measuring the gravity-field gradient are increased measurement stability, rejection of common mode and vibrational noise, increased resolution due to a higher decay rate of the gradient field, and higher spatial sampling.

Whereas gravity is measured in units of acceleration (meter per square second), the gradient of gravity is measured in per square second. A unit reflecting the commonly encountered magnitude is eötvös, which is given by

$$1 \text{ eötvös} = \frac{10^{-9}}{\text{s}^2} = \frac{10^{-4} \text{ mGal}}{\text{m}}.$$

Current gravity gradiometers can have an instrument noise level of less than 1 eötvös during stationary data acquisition [11]. One measurement can include gradients of all three Cartesian components of the gravity field to form a second-order tensor whose elements are the second partial derivative of gravity potential Φ, i.e.,

$$\mathbf{T} = \nabla\nabla\Phi = \begin{pmatrix} \left[\frac{\partial^2\Phi}{\partial x^2}\right] & \left[\frac{\partial^2\Phi}{\partial x \partial y}\right] & \left[\frac{\partial^2\Phi}{\partial x \partial z}\right] \\ \frac{\partial^2\Phi}{\partial y \partial x} & \left[\frac{\partial^2\Phi}{\partial y^2}\right] & \left[\frac{\partial^2\Phi}{\partial y \partial z}\right] \\ \frac{\partial^2\Phi}{\partial z \partial x} & \frac{\partial^2\Phi}{\partial z \partial y} & \frac{\partial^2\Phi}{\partial z^2} \end{pmatrix}. \quad (1)$$

The gravity potential is harmonic and well behaved outside source regions. Consequently, $\mathbf{T}$ is symmetric and traceless. Thus, only the five components that are indicated by brackets are independent. Furthermore, a recovered model can be constructed through the inversion process with any one component of $\mathbf{T}$. Additional components both increase the signal-to-noise ratio and provide further independent spatial information on the

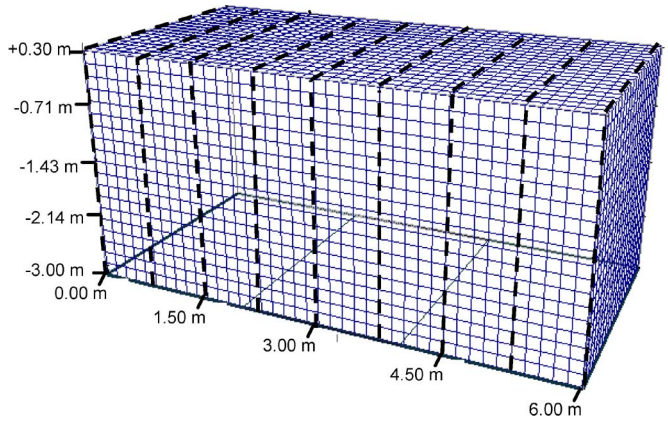

Fig. 2. Mesh of the cargo container with the projections of gravity-gradiometry sensor gate locations onto the container that are indicated by dark black lines. The sensor gate is constructed from an array of sensors stacked on top of each other (on the sides) and next to each other (on the top). On the top and sides, the sensors are separated by 0.60 m, which was chosen based on the size of the commercially based sensors. As the container is pushed through the gate, we propose acquiring data every 0.30 m, although the lengthwise data spacing can be increased at the cost of additional acquisition time.

source density. $\mathbf{T}$ that is produced by a point source is related to the mass by

$$\mathbf{T} = \gamma m \nabla\nabla \frac{1}{|\vec{r} - \vec{r}_0|} = \gamma m \Gamma \quad (2)$$

where γ is the gravitational constant, which is equal to 6.672×10^{-8} m^3/g/s^2; Γ is the dyadic Green's tensor; $\vec{\mathbf{r}}_0$ is the sensor location; and $\vec{\mathbf{r}}$ is the source location. The gravity gradient due to distributed mass that is characterized by a density function can be derived using (2).

III. Inversion Algorithm to Construct Density Distribution

The cargo container is divided into a set of prismatic cells by using a 3-D orthogonal mesh and assuming a constant density within each cell (Fig. 2). Given this discretization, a particular component of the gradient tensor at a given observation location, which is denoted as the ith datum d_i, can be written as

$$d_i = T_{KL} = \sum_{j=1}^{M} \rho_j \left\{ \iiint_{V_j} \frac{\partial^2}{\partial x_K \partial x_L} \frac{1}{|\vec{r} - \vec{r}_0|} dV \right\}$$
$$= \sum_{j=1}^{M} \rho_j \mathrm{G}_{ij}. \quad (3)$$

In (3), ρ_j and V_j are the density and volume of the jth cell, respectively, and G_{ij}, which is defined by the expression in braces, quantifies the contribution of the jth model cell to the ith datum. M is the number of model cells, and K and L are the indices referring to the axis directions in the Cartesian coordinate system. Expressed in matrix notation, the gravity-gradient data consisting of N observations are given by

$$\vec{d}_{\text{obs}} = \mathbf{G}\rho + \vec{\varepsilon} \quad (4)$$

where $\vec{d}_{\rm obs}$ is the measured data vector, ε are the measurement errors, $\mathbf{G}$ is the sensitivity matrix whose elements are G_{ij} (3), and $\vec{\rho}$ is a model vector of spatially distributed density values. $\mathbf{G}$ contains the physics and geometry of the problem and represents the mapping from model space to data space. We seek to minimize $\mathbf{G}\,\vec{\rho} - \vec{d}_{\rm obs}$ by finding $\vec{\rho}$ that predicts important aspects of the data and is physically realistic.

The standard approach to solving this problem uses the L_2 norm with some degree of regularization [12]. Anscombe [13] discussed the idea behind regularization as a measured sacrifice of model performance for stabilization that is caused by reasonable deviations from such model. We choose to set up the inversion problem with a Tikhonov regularization approach [14] by constructing a model objective function for the recovered model $\vec{\rho}$, using a data misfit to measure the fit of the predicted data to the measured data, and choosing an optimal regularization parameter that combines the two quantities. Li and Oldenburg [15], [16] and Li [17] discuss the merits of a particular model objective function in potential field theory applications, which we generalize to the following form for this paper:

$$\begin{aligned}\phi_m(\rho) =& \alpha_S \iiint_V w(\vec{r})|\overline{\rho}(\vec{r})|^p dV \\ &+ \alpha_x \iiint_V w(\vec{r}) \left|\frac{\partial \overline{\rho}(\vec{r})}{\partial x}\right|^p dV \\ &+ \alpha_y \iiint_V w(\vec{r}) \left|\frac{\partial \overline{\rho}(\vec{r})}{\partial y}\right|^p dV \\ &+ \alpha_z \iiint_V w(\vec{r}) \left|\frac{\partial \overline{\rho}(\vec{r})}{\partial z}\right|^p dV. \end{aligned} \tag{5}$$

In (5), $w(\vec{r})$ is a model cell-specific weighting term. The α parameters allow the user to choose the type of model. For example, increasing values of α_x, α_y, and α_z provide smoother recovered models in respective dimensions, whereas increased α_s attempts to minimize the amplitude of the model. We also develop cell weighting in $\mathbf{G}$ from (4), which is used to compensate model cells with different distances from observation locations [18]. Since the gravity-gradiometric field decays with the inverse of the distance cubed [18], if the distance from the source were not compensated, the cells that are closest to the observation location would dominate in reproducing data through (3). In this scenario, the recovered model would have all the density in the model cells that are closest to the surface of the container.

In addition, whereas (5) does not explicitly state that there may be a reference model, such a model, i.e., $\vec{\rho}_0(\vec{r})$, can simply be subtracted from $\vec{\rho}(\vec{r})$ within the model objective function [15]. Different choices of exponent $p \in [1, \infty)$ in (5) define different measures for the complexity of the model. When $p = 2$, (5) is the mean square estimator or L_2 norm. If $1 \leq p \leq 2$, (5) is characterized as a robust estimator, and we examine the details in a later section.

The additional component for an inversion using the formalism of Tikhonov regularization is a measure of the difference between observed and predicted data, i.e., the data misfit, given by

$$\phi_d = \left\| \mathrm{W}_d(\mathrm{G}\,\vec{\rho} - \vec{d}_{\rm obs}) \right\|^p \tag{6}$$

where $\vec{d}_{\rm obs}$ is the measured data and W_d is a diagonal matrix whose ith element is $1/\sigma_i$, where σ_i is the standard deviation of the ith datum. The assumption that noise in $\vec{d}_{\rm obs}$ is uncorrelated allows only diagonal terms in W_d. We choose to use uncorrelated Gaussian noise for simplicity. The appropriate exponent in (6) is $p = 2$. The results that are presented here hold true when different noise models and corresponding statistics are used in the simulation. Combining (5) and (6) with a regularization parameter μ provides a global objective function

$$\phi = \phi_d + \mu\phi_m. \tag{7}$$

The regularization parameter controls the relative importance of data misfit to the model objective function [19]. ϕ_d is a chi-squared random variable that is distributed with N degrees of freedom, where N is the number of observation data. The expected value for the data misfit is then N, which defines a target misfit to be achieved in the inversion [15].

The inverse solution for this problem is then obtained by finding a model $\vec{\rho}(\vec{r})$ that minimizes ϕ_m in (7) and misfits the data by ϕ^* [20]. The specific algorithm for carrying out the minimization depends on the value of p and on other constraints that we may desire to impose on the problem [21].

The most common approach in geophysical inversion is to use a value of $p = 2$ in (5), which yields a mean-squared estimator. For a numerical solution, we discretize (5) using the same mesh as the forward modeling in (3) and by a finite-difference approximation to produce the following matrix form:

$$\begin{aligned}\phi_m(\rho) =& \vec{\rho}^{\,T}\mathrm{W}_S^T\mathrm{W}_S\,\vec{\rho} + \vec{\rho}^{\,T} \\ &\times \left(\mathrm{W}_X^T\mathrm{W}_X + \mathrm{W}_Y^T\mathrm{W}_Y + \mathrm{W}_Z^T\mathrm{W}_Z\right)\vec{\rho} \\ \equiv& \vec{\rho}^{\,T}\mathbf{W}^{\mathbf{T}}\mathbf{W}\,\vec{\rho}\,. \end{aligned} \tag{8}$$

The constructed model will then be characterized by a smooth transition between regions with different density values.

There is an important distinction between applying the L_P norm to the data misfit in (6) and applying the same norm to the model objective function in (5). Applied to the data misfit, solutions reflect the relative importance of each datum that is fundamentally determined by the distribution of the specific L_P norm. However, applied to the model objective function, solutions reflect the ability of a recovered model to contain significantly different parameter values in adjacent model cells, which is fundamentally determined by the distribution of the specific L_P norm. Thus, varying p in (6) affects the weighting of outliers in data space, but varying p in (5) determines the ability of adjacent cells to incorporate large jumps in model space. As we are not concerned with data outliers in this paper, $p = 2$ in (6) for computational simplicity.

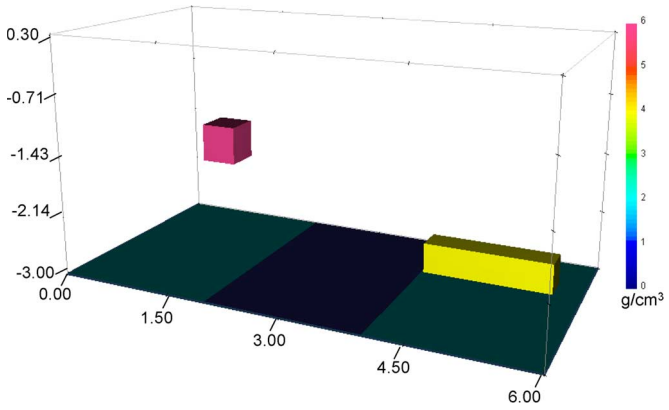

Fig. 3. Model that is used to produce the data set that is inverted in this paper. A Gaussian noise of 2% at a minimum of 1 eötvös is added to the data prior to inversion. The left block is a plutonium ($\rho = 19$ g/cm^3) pit with volume equal to one model cell (which is chosen to be 15 cm^3 for this example), which is surrounded by an outer lead ($\rho = 11$ g/cm^3) annulus of one-model-cell thickness, which in turn is surrounded by a packaging material ($\rho = 0.6$ g/cm^3) of one-model-cell thickness, resulting in an average density of approximately 6 g/cm^3. The horizontal bar on the right is depleted uranium in low-density packaging with an average density of 4.0 g/cm^3. The density units are grams per cubic centimeters.

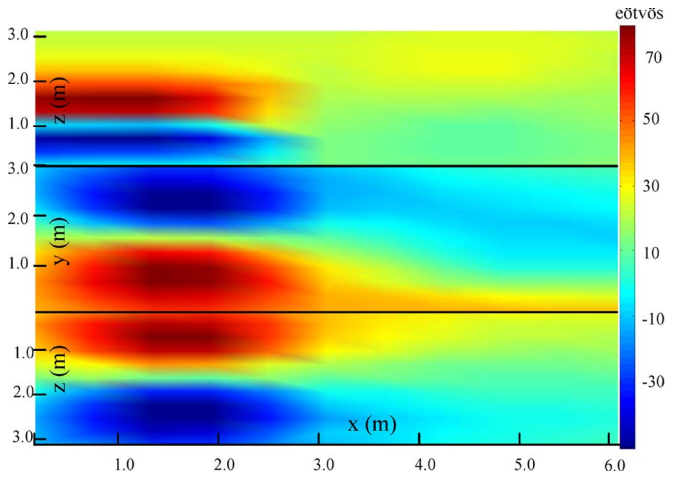

Fig. 4. T_{YZ} component of synthetic gradiometry data computed with (4) using the true model in Fig. 3. To interpret, start with an aerial view (XY plane) of Fig. 2 from the vertical axis. Upward fold the two sides of the cargo container, so that they are now coplanar with the XY plane. The top frame is therefore the data from the sensors on the far end of the sensor gate, as shown in Fig. 1, the middle frame is the data that are acquired from the horizontal top bar of the sensors, and the bottom frame is the data from the near-side sensors. The color bar units are eötvös.

A. *Bound-Constrained Inversion With Mean-Square Estimator*

In order to recover a realistic density distribution, we choose to impose bound constraints that density values be positive and have an upper bound. Fig. 3 shows that the chosen model of a plutonium ($\rho = 19$ g/cm^3) pit with volume equal to one model cell (15 cm^3 for this example) is surrounded by an outer lead ($\rho = 11$ g/cm^3) annulus that is also of one-model-cell thickness, which is surrounded by a packaging material ($\rho = 0.6$ g/cm^3) of one-model-cell thickness, resulting in an average density of approximately 6 g/cm^3. The lower and upper bounds are thus set to 0.0 and 6.0 g/cm^3, respectively. These bound constraints can be enforced during inversion and optimization using transformation methods [22], interior point methods [23], [24], and several quadratic programming methods [25]. In this paper, we use a primal logarithmic barrier technique [23], which is a class of interior point methods. In this method, the bound constraints are enforced through a logarithmic term that acts as a barrier to prevent the solution from reaching over to the infeasible domain (i.e., negative or above the upper bound). The objective function then assumes the following form:

$$\phi(\lambda) = \phi_d + \mu\phi_m - 2\lambda \left[\sum_{j=1}^{M} \ln \frac{\rho - \rho^{\min}}{\rho^{\max} - \rho^{\min}} + \ln \frac{\rho^{\max} - \rho}{\rho^{\max} - \rho^{\min}} \right] \tag{9}$$

where $\rho^{\min}$ and $\rho^{\max}$ are the lower and upper bounds, respectively, and λ is referred to as the barrier parameter.

The first two terms have a quadratic relationship to the model parameters since the relationship between gravity gradient and density values in the cells is linear. However, the logarithm term of (9) causes the total objective function to be nonquadratic. In addition, the logarithmic barrier method requires that a sequence of minimization problems with decreasing λ be solved, and the final solution is given when $\lambda \to 0$. For these reasons, (9) is solved iteratively. We start with a large λ and take a Newton step at each iteration while simultaneously decreasing λ in subsequent iterations. Further details of this optimization and the derivative terms of (9) can be found in [18] and [19]. When carrying out the logarithmic barrier solution, μ is held constant in (9). A complete inverse solution typically is preceded by a line search for optimal μ through several trial values.

To illustrate our construction algorithm, we use a synthetic model that is shown in Fig. 3, which simulates a container with a packaged plutonium pit and a packaged depleted uranium rod. This plutonium and uranium model is used to produce the simulated data set for this paper. Since the gravity-gradient signal has a range of more than 100 eötvös (Fig. 4) and the noise level of stationary gravity gradiometers is stated to be below 1 eötvös [11], 2% Gaussian noise applied in this model is a reasonable estimate. As an illustration, Fig. 4 displays one component (T_{YZ}) of the gravity-gradiometry response. Throughout this paper, we have used all five independent components of the gradient tensor. We note that the gradient data are sampled discretely over limited areas in 3-D space, so each component does bring additional independent information. A single component of data will produce good results, but multiple components are generally superior. We apply the inversion algorithms that are presented in this paper to these data to produce different density models (Figs. 5 and 7).

Fig. 5 shows the recovered model from using a mean-square estimator and bound constraints. Although this image identifies the high-density zones within the cargo container reasonably well, the boundaries are blurred, which causes the amplitude of the density anomaly to be rather small. This blurring effect, which is well known in geophysical inversion [26] and the image processing community [27], arises because the constructed model from a mean-square estimator approximates sharp boundaries by a sequence of small steps that are spread over an interval. It is the mean-squared estimator that,

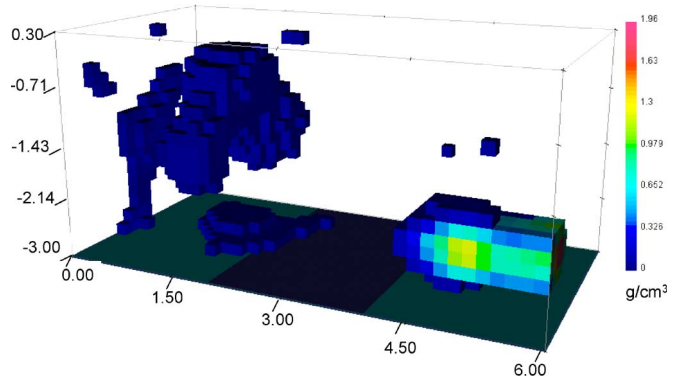

Fig. 5. Density model that is recovered from the true model in Fig. 3 using $p = 2$. Bound constraints are enforced in this example in the interval of $0.0-6.0$ g/cm^3. The lowest 2% of recovered density values are not plotted.

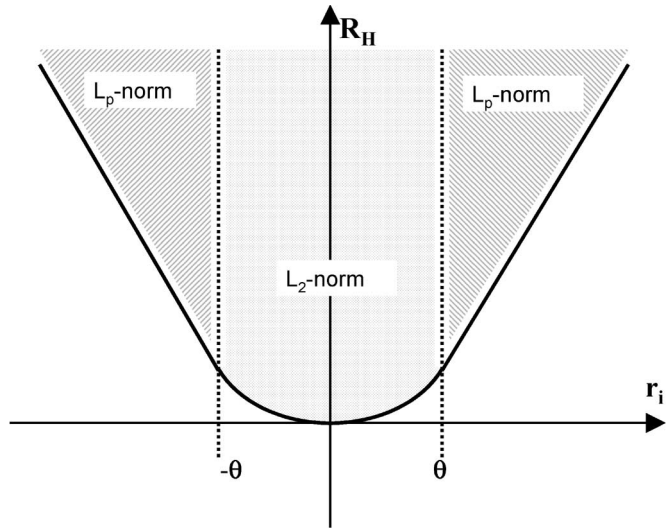

Fig. 6. Distribution of recovered models and their respective norms from an arbitrary example. The purpose of a Huber norm is to condition a distribution with the potential for singularities to one that is computationally stable. A threshold θ is defined such that models having a residual of less than θ are estimated by the mean-square estimator $(p = 2)$, whereas all models with a residual of greater than θ are estimated with a robust estimator $(p = 1)$. Thus, as we approach a singularity (the vertical axis) and $r_i \rightarrow \infty$, we switch the values of r_i in (16). θ is a function of data quality, degree of sensor coverage, expectation of sharply recovered boundaries, and estimation of resolution.

when applied to the model derivatives, acts to suppress large differences between adjacent cells. To construct models with larger differences and therefore sharper boundaries, we next investigate robust estimators.

B. Bound-Constrained Inversion With Robust Estimator

The proposed gradiometry system is stationary, which creates low instrument noise levels and effectively prevents data outliers. We therefore retain the mean-square estimator for data misfit (6) and concentrate on the application of robust estimators for the model objective function. Robust estimators are based on the median of the model differences [28], whereas the mean-square estimator is based on the mean of the model differences [29]. As previously stated, the median-based approach will preserve the large model differences that are crucial for recovering sharp boundaries.

An attempt to apply the chosen solution method $1 \leq p < 2$ can be made at this point, but a numerical difficulty quickly appears. When $p \neq 2$, the model objective function is nonquadratic. More specifically, the solution involves quantities such as $|\delta\rho|^{p-2}$, where $\delta\rho$ is the difference between adjacent cells, thus creating singularities when the model differences approach zero during the optimization.

These singularities can be addressed using one of several methods [30], [31]. Strictly for $p = 1$, the most appropriate of these might be to recast the problem into an equivalent linear programming problem. Alternatively, iteratively reweighted least squares, which solve a sequence of least squares problems with recursively computed weighting matrices, also provide an approximation to the l_1 solution [30].

However, the solution to the problem of singularities that arises when $1 \leq p < 2$ requires a more general approach. We choose to define threshold θ, which establishes a minimal acceptable value for the difference without causing numerical instability. θ is determined experimentally and is platform and problem specific. If the model difference is between zero and the defined threshold, a mean-squared estimator $(p = 2)$ is used. If the model gradient residual is greater than the threshold, the robust estimator is used $(1 \leq p < 2)$.

The Huber norm [19], [28] is such a measure that satisfies our needs, i.e.,

$$\mathbf{R}_H = \begin{cases} \frac{(\delta\rho)^2}{2}, & |\delta\rho| \leq \theta \\ \theta|\delta\rho| - \frac{\theta^2}{2}, & |\delta\rho| > \theta. \end{cases} \tag{10}$$

With the derivatives of (10) defined as a series of weights,

$$w_H(r_i) = \begin{cases} 1, & |r_i - \delta\rho| \leq \theta \\ \theta|\delta\rho|^{-1}, & |r_i - \delta\rho| > \theta. \end{cases} \tag{11}$$

Weights w_H then modify the model objective function by operating between W^T and W in (8).

A conceptual explanation of the Huber norm for $p = 1$ is illustrated in Fig. 6. Note that the Huber norm is not a mathematical norm [32] but a mathematical function operating on a distribution. In addition, note that both sides of the threshold are defined in (10), so that the measure and its derivative in (5) are now continuous. Although the second derivative of (10) is discontinuous, this does not generally result in stability concerns.

The Huber norm provides two advantages: 1) It removes the singularities that are caused by the use of a robust estimator. 2) It maintains the large model differences that are required for sharp density discontinuities in the recovered model. Fig. 7 is the inverted image with a robust estimator, i.e., $p = 1$, applied to the model objective function, with applied bound constraints and the use of the Huber norm. The recovered density model has noticeably sharper boundaries.

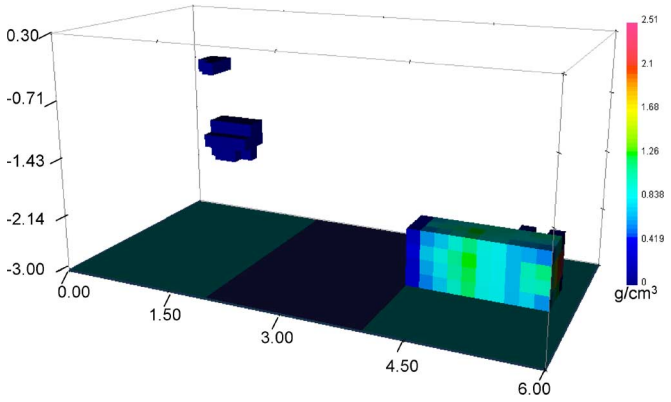

Fig. 7. Density model that is recovered from the true model in Fig. 3 using $p = 1$ and $\theta = 1.0 \times 10^{-8}$. Bound constraints are enforced in this example in the interval of $0.0-6.0$ g/cm^3. The lowest 2% of recovered density values are not plotted. Note the higher recovered density values with the bound constraints and $p = 1$. In a more realistic situation, we would expect more mass in the trailer, which will result in higher recovered densities.

IV. Appraisal of Recovered Models

Nonlinear model appraisal in the geoscience community [33] primarily focuses on the variance and resolution of recovered models. Variance analysis quantifies how errors in the measured data are mapped into the recovered model, while resolution analysis quantifies the ability of the recovered model to successfully identify separate features or to quantify individual features. The resolution is studied through the formation of both linear and nonlinear model resolution matrices to determine the spatial precision to which individual model parameters can be recovered. Variance analysis for nonlinear model appraisal can be accomplished through several methods, including the covariance matrix [34], [35], the Cramer–Rao (CR) bound [36], [37], and funnel analysis. The covariance matrix indicates how measured data errors are correlated between model parameters, while the CR bound calculates the lower bound for any estimate of a nonrandom parameter. The CR bound is an intriguing subject for future study partly because the requisite second derivative of the log likelihood function is already explicitly calculated through the Hessian matrix in the optimization of (7). However, as the critical focus in this nonlinear model appraisal is detection, funnel analysis is chosen because it offers the absolute maximum and minimum bounds of a model parameter as a function of volume.

A. Funnel Analysis

A primary interest is to determine whether a high-density volume that is recovered from inversion is likely to indicate fissile material. This section uses a type of bound analysis, which is called funnel analysis, to characterize the uncertainty in the recovered inversion models [38]. The results of such an analysis are a function of the quality of sensor coverage, the mass distribution of the container, and the presence of sharp density contrasts within the container.

Given a data set $\vec{d}_i$ $(i = 1, \ldots, N)$, we perform an initial bound-constrained inversion. It is necessary to next identify the region of highest recovered density with the assumption that if fissile materials are present, they will have the highest density in the container. This region, which is defined as V_{SI}, is the starting point for funnel analysis and is defined by discarding the lowest 98% of the recovered model cell density values, with the density threshold value having been determined experimentally. In the example of the plutonium pit that is shown in Fig. 7, this starting region contains 27 $(3 \times 3 \times 3)$ cells.

In the funnel analysis, we compute the lower and upper bounds on the average density in a given region within the model domain. Each lower and upper bound is defined as the minimum and maximum mean density of all the models that fit the data to the same degree, as determined by the data errors. Each bound is calculated by carrying out an inversion to generate an extreme model that either minimizes or maximizes the density in the selected region while ignoring the complexity of the model in other regions. Within region V_{SI}, this is described in [39]. For the lower bound, we solve

$$\min \phi_m = \int_{V_{\mathrm{SI}}} |\rho| dv \quad \text{such that } \phi_d = \phi^*. \tag{12}$$

For the upper bound, we solve a maximization problem

$$\max \phi_m = \int_{V_{\mathrm{SI}}} |\rho| dv \quad \text{such that } \phi_d = \phi^* \tag{13}$$

which can be solved by an equivalent minimization problem

$$\min \phi_m = \int_{V_{\mathrm{SI}}} |\rho - \rho_0| dv \quad \text{such that } \phi_d = \phi^* \tag{14}$$

and when ρ_0 is large (e.g., 100).

ϕ^* is the same misfit expectation value that is discussed in the previous section. Equations (12) and (14) are subject to density-bound constraints of 0.0 and 6.0 g/cm^3 that are applied in order to recover a reasonable model. Calculation of the first set of bounds is accomplished by defining $V_{\mathrm{S}(1)}$ as a single cube at the center of the region of high density. The next set of bounds results from defining $V_{\mathrm{S}(2)}$ as a larger symmetrical cube that is centered on $V_{\mathrm{S}(1)}$. $V_{\mathrm{S(n)}}$ is the largest cube in this paper. The curves in Fig. 8 represent the size of this region as a function of characteristic volume, and the abscissa equals $V_{\mathrm{S(n)}}$ that is normalized by the total volume of interest.

As defined in (12)–(14), only within V_{SI} is the model objective function defined; the volume outside V_{S1} only contributes to the data misfit. In the limit, as V_{SI} approaches the size of the entire model, the minimum and maximum mean density values converge to the total model density. Once each pair of optimization problems is solved, we compute the average densities within V_{SI} and use them as the upper and lower density bounds.

Fig. 8 plots the results, in two different axis configurations, for the synthetic model that is shown in Fig. 3. Given a volume of interest in the recovered model, the true density of that volume can be any value between the corresponding upper and lower bounds in Fig. 8. Whether we consider the total mass or the average density of the recovered plutonium pit as a

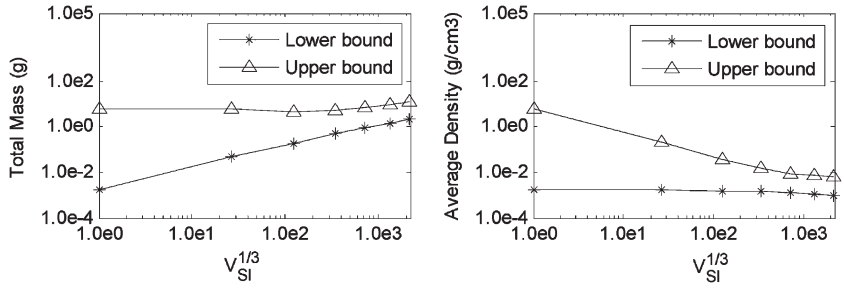

Fig. 8. Results of funnel analysis on a plutonium ($\rho = 19$ g/cm^3) pit with volume equal to one model cell, which is surrounded by an outer lead ($\rho = 11$ g/cm^3) annulus of one-model-cell thickness, which in turn is surrounded by a packaging material ($\rho = 0.6$ g/cm^3) of one-model-cell thickness. The average density of this model is approximately 6.0 g/cm^3. The analysis considers a maximum volume of $V_{\rm SI} = 2182$ cells out of the total number of model cells, i.e., 15 200. The smallest volume contains 27 cells. The two plots result from density bounds that are enforced in inversion, which are bounded between 0.0 and 19.0 g/cm^3. In each plot is the upper limit of $V_{\rm SI}$ from (19) and the lower limit of $V_{\rm SI}$ from (17). The left plot shows the total mass within $V_{\rm SI}$, while the right plot shows the average density within $V_{\rm SI}$. Clearly, the variance of the true average density increases with decreasing volume size. For this reason, a plutonium pit can be detected with gravity-gradiometric imaging, but nothing certain can be ascertained regarding the exact value of the recovered density. Larger bodies produce less variance, and more can be said about their recovered densities.

function of volume, the analysis is unaffected. If one interprets the plutonium to be highly resolved within one cell in the recovered model, the far left of each plot in Fig. 8 shows that the true density of that model cell could vary between less than 1.0×10^{-2} and 19.0 g/cm^3. However, if one interprets the plutonium location as less compact, perhaps spreading into 125 model cells, the variance is reduced, thus illustrating the tradeoff between resolution and variance in model appraisal. In the cargo-container-imaging problem, we seek to detect the presence of high-density spatially compact materials, such as plutonium, which would ostensibly occupy less than 125 model cells in the discretization of Fig. 3. Yet, for small volumes, Fig. 8 shows a vast density range in which the true density can lie. This leads directly to a fundamental limitation in imaging cargo containers with the gravity-gradiometry technique; nonlinear inversion can recover areas of high density that are likely to be indicative of spatially compact fissile materials but can provide no certainty on the recovered density of such materials. Complementary inspection techniques must be then used for confirmation of fissile material.

B. Construction of Unconstrained (Linear) and Bound-Constrained (Nonlinear) Resolution Matrices

Inversion of a gravity-gradiometry data set d_i attributes a set of gravity-gradient density measurements to a distribution of mass, which best reproduce the data set according to the error tolerance. This recovered density distribution $\vec{\rho}$ can never perfectly resolve the true model due to nonuniqueness, data noise, prior assumptions, and roundoff error [40]. Assumptions, even the least obvious, such as discretization, can also contribute to the difference between the recovered and true models. The primary effect of these assumptions and limitations on the recovered model is that the edge, or boundaries, of the recovered density tends to be a diffused zone of transition. The proposed use of the Huber norm in the previous section limits the spreading effect through the use of robust estimators, but it will not eliminate the spreading completely. The attempt in the previous section to limit the spreading effect through the use of robust estimators is now followed by studying the spreading effect through the use of the resolution matrix. The underlying physics and geometry of the imaging problem determine the resolution matrix, as does the choice of model regularization μ in (9), due to data noise levels and sensor coverage.

Alumbaugh and Newman [41] apply linearized model covariance and resolution matrices to determine resolution and parameter estimation accuracy for nonlinear inversions. Alumbaugh [42] uses covariance estimation techniques to understand the inherent differences between linearized solution estimation and full nonlinear solution estimation. In addition, Alumbaugh and Newman [41] discuss resolution on spatial location that is estimated with model resolution and model covariance matrices. Routh *et al.* [43] forms the resolution matrix for crosswell tomography applications in order to appraise the results of optimizing sensor placement. This prior research is significant because, for realistic large problems, it is not practical to execute the inversion with a direct method such as SVD [44], where the resolution matrix is explicitly formed. However, SVD has been successfully used on smaller problems to form the resolution matrix [35]. For this reason, conjugate gradient is one alternate solution method that is used widely. The conjugate-gradient method has the advantage of being able to solve large problems since the required matrix-vector multiplications are obtained implicitly and in turn leads to the disadvantage of not being able to explicitly form the model resolution matrix.

Model resolution matrix $\mathbf{R}$ relates the true model to the recovered model, i.e.,

$$\vec{\rho}_R = \mathbf{R}\vec{\rho}_T + \Delta\vec{\rho} \tag{15}$$

where $\vec{\rho}_R$ and $\vec{\rho}_T$ are the recovered and true models, respectively, and $\Delta\vec{\rho}$ is a model bias and noise term. Inclusion of the last term in (15) is necessary for consistency because, while $\vec{\rho}_R$ is a random variable, $\mathbf{R}$ and $\vec{\rho}_T$ are not. $\mathbf{R}$ is a square matrix with dimensions that are equal to the number of model cells. $\mathbf{R}$ is also asymmetric, which leads to a conceptual difference between the rows and columns [39]. The rows are averaging functions such that each cell in the recovered model is a weighted average of the true model, whereas the columns

are the point spread functions that quantify the manner in which an impulse in the true model spreads to other regions in the recovered model. A quantitative analysis of the differences between rows and columns, or correspondence analysis [45], should be a valuable tool in resolution appraisal and is the subject of a separate investigation.

As the conjugate-gradient method is used for the solution, one must form $\mathbf{R}$ accordingly. To accomplish this, we form $\mathbf{R}$ through a series of single inversions in the following manner. First, examine the resolution matrix in the case of unconstrained inversion with a quadratic model objective function. For the quadratic and unconstrained problem, the recovered model can be written as

$$\rho_R = \mathrm{H}^{-1} G^T \mathrm{W}_d^T \mathrm{W}_d \vec{d}_{\mathrm{obs}} \tag{16}$$

where H^{-1} is the inverse of the Hessian matrix without the logarithmic terms, i.e., $\mathrm{H} = \mathrm{G}^T\mathrm{G} + \mu \mathrm{W}^T\mathrm{W}$.

Substituting the data equation $\vec{d}_{\mathrm{obs}} = G\vec{\rho} + \vec{\varepsilon}$ into (16) yields the definition of the resolution matrix for this simple case, i.e.,

$$\begin{aligned}\rho &= \mathrm{H}^{-1} G^T \mathrm{W}_d^T \mathrm{W}_d G\vec{\rho} + \mathrm{H}^{-1} G^T \mathrm{W}_d^T \mathrm{W}_d \vec{n} \\ &\equiv R\vec{\rho} + \Delta\vec{\rho}\,. \end{aligned} \tag{17}$$

This equation also provides the means to construct the resolution matrix without forming the inverse of Hessian H^{-1} explicitly. Suppose that we have a true model that consists of only one cell corresponding to the jth model cell,

$$\vec{\rho}_T^{\,j} = (0, \ldots, 0, 1, 0, \ldots, 0)^T\,. \tag{18}$$

Substituting $\vec{\rho}_T^{\,j}$ to (17) results in a recovered model $\vec{\rho}_R^{\,j}$ that is the corresponding jth column of the model resolution matrix. Note that the noise term $\vec{n}$ is no longer present. Although (16) cannot be evaluated explicitly since there is no analytic explicit expression for H^{-1}, it can be obtained by performing one inversion to the data that are produced by the impulsive model $\vec{\rho}_T^{\,j}$, i.e.,

$$\vec{d}_{\mathrm{obs}}^{\,j} = G\vec{\rho}_T^{\,j} \tag{19}$$

according to (16). Performing M inversions with M difference impulsive models therefore completes the resolution matrix; again, there are M discretized model cells.

The formation of $\mathbf{R}$ to nonquadratic and bound-constrained problems can be accomplished using the same approach. However, there is no explicit inverse operator since it is defined by the inversion process that incorporates nonlinear parts such as bound constraints and a nonquadratic model objective function. The advantage is that the resolution matrix can be constructed whenever we perform the inversion with minimal additional computation cost. This method applies whether the inversion is carried out by an explicit method, such as SVD, or an implicit and iterative approach, such as the conjugate-gradient method. In this current problem, we note that the Hessian matrix in (16) becomes model dependent due to the logarithmic terms at each iteration and that each inversion must be carried out by going through the entire logarithmic barrier iteration. This is the manner in which bound constraints are incorporated into the resolution matrix. In the nonquadratic $\mathbf{R}$ construction, we also use a robust estimator, which is accounted through the changing model weighting matrix for each iteration. In other words, since the constrained inversion allows us to obtain each column of the resolution matrix, the effect of the robust estimator on the resolution matrix is accounted for automatically. To summarize the formation of the resolution matrix, for any given data set, the chosen estimator, bound constraints, and optimal regularization parameters collectively define the inverse operator, which is mathematically represented explicitly or implicitly. Application of this inverse operator to the data yields the recovered model. This same inverse operator can then be applied to data sets that are produced by an impulse model, which is described in (18), to obtain the model resolution matrix.

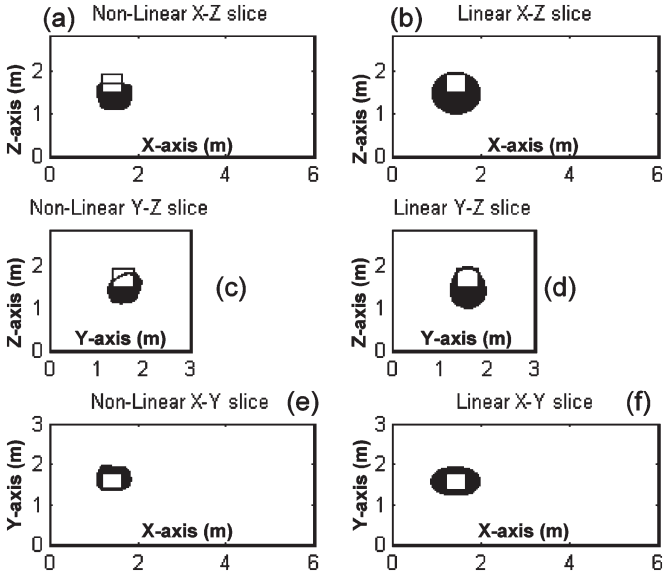

Fig. 9. Three orthogonal slices through the column of resolution matrix $\mathbf{R}$ corresponding to the center of the plutonium pit shown in Fig. 3. All dimensions are expressed in meters. Each subplot has a black area that contains the recovered density within 1.0 standard deviation of the maximum recovered density value. The white square in each figure is the location of the original plutonium cube in each dimension. Each axis is the cargo-container dimension of the plane in meters. Note the (a) X-plane, (c) Y-plane, and (e) Z-plane slices for the nonlinear inversion when $p = 1$ and bound constraints of 0.0 g/cm^3 (lower) and 6.0 g/cm^3 (upper) are applied. In addition, note the (b) X-plane, (d) Y-plane, and (f) Z-plane slices for the linear inversion when $p = 2$ and no bound constraints are used. For $p = 2$, the recovered density appears to be centered in the X and Y planes but biased toward greater depth in the Z plane. The resolution image for $p = 1$ is improved but is asymmetric.

In the example that is used in the funnel analysis, a shielded plutonium pit (the left model block in Fig. 3), we construct both linear and nonlinear $\mathbf{R}$ matrices. Each row or column of the $\mathbf{R}$ corresponds to a model in three dimensions. We display each row or column in the format of a model either by volume rendering or by slices. Three spatially orthogonal slices of the column intersecting the center of the plutonium pit are shown in Fig. 9 for the constrained resolution matrices when $p = 1$ and $p = 2$. More detailed plots of the differences between $p = 1$ and $p = 2$ are shown in Fig. 10. In Fig. 9, we plot only the recovered

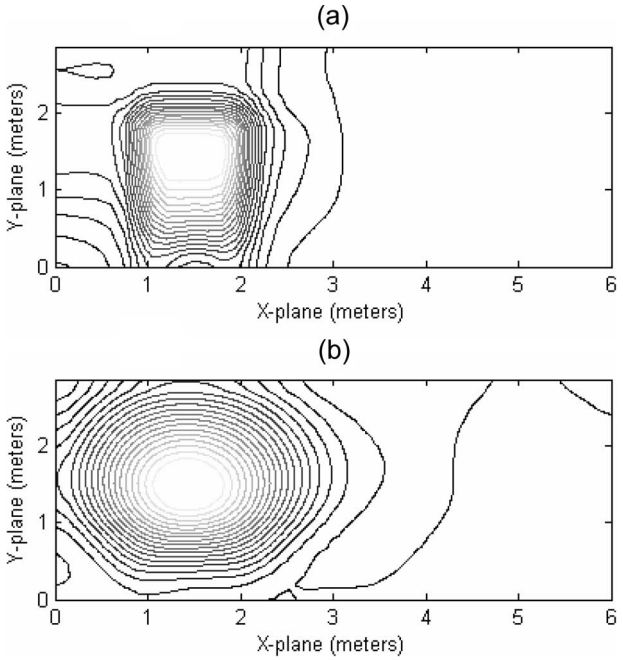

Fig. 10. Contour X–Y slices through the column of resolution matrix $\mathbf{R}$ corresponding to the center of the plutonium pit in Fig. 3. All dimensions are expressed in meters. (a) The upper contour is the X–Y model plane when $p = 1$ and bound constraints [0.0−6.0 g/cm^3]. (b) The lower contour is the X–Y model plane when $p = 2$ and no bound constraints are applied. Note the effect of setting $p = 1$ on recovering sharp boundaries. Contour values are not shown in order to accentuate on the contour shape.

model cell densities above 1.0 standard deviation of the values in model space. The choice of using standard deviation as a measure, although arbitrary, arises from the need to quantify the relative, and not the absolute, amplitudes of a slice through $\mathbf{R}$. In Fig. 9, the recovered density above the threshold is plotted as the black region, whereas the white box is the true model of the plutonium pit. Recovered models tend to have skewed depth resolution but higher resolution in the Y-horizontal plane, which results from uneven sensor configuration. The nonlinear $\mathbf{R}$ is characterized by a higher resolution than the linear $\mathbf{R}$ due to the realistic bound constraints and robust estimator. The asymmetry in Fig. 9(a), (c), and (e) will be discussed in a future paper.

Density inversion using gravity-gradiometry data is a linear process. We can thus understand the resolution matrix without the complication of nonlinearity. Yet, by including the presence of nonlinear bound constraints and modifying the distribution of the model objective function to achieve sharp edge recovery, we can provide insight into the structure and statistical nature of the nonlinear resolution matrix. Furthermore, resolution matrices resulting from a mean-squared-estimator-based inversion appear to have a distinctly different distribution from resolution matrices resulting from robust estimators such as the Huber norm. We relate the distribution of the model objective function to the estimator distribution in future research.

C. Analysis of Model Appraisal

The funnel analysis clarifies the tradeoff between resolution and variance [46]. A smaller recovered anomaly volume implies a larger variation of density. Larger recovered anomalies have improved variance but decreased resolution. Whereas the example in this paper focuses on a small fissile body, the variance and resolution are increased for larger trailer masses with smaller density contrasts.

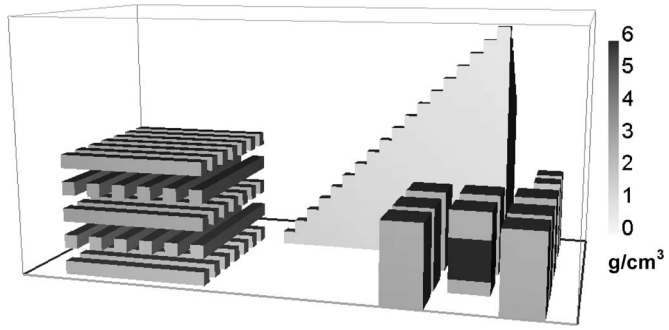

Fig. 11. Experimental validation of the inversion and model appraisal methods that are discussed in this paper using a more complicated example. This model has the same geometry, sensor coverage, and noise levels as in Fig. 3, yet has more clutter and uniform, instead of Gaussian, noise added to the forward solution. The packaged plutonium ($\rho = 6.00$ g/cm^3), which appears in black on the front right, is concealed in one of eight barrels of metallic scrap ($\rho = 3.20$ g/cm^3) that are separated by 0.15 m. Alternately stacked aluminum rods ($\rho = 2.20$ g/cm^3) are on the left side of the model. A wooden construction form ($\rho = 0.75$ g/cm^3) is at the rear center of the container.

Funnel analysis on the plutonium pit example and others that are not discussed in this paper suggest that we are unlikely to detect fissile material that is smaller than about 15 cm^3. Relying on robust estimators and bound constraints, we should expect the resolution of a 15-cm^3 plutonium pit to be spread over a volume of at least 45 cm^3 in the Y axis and at least 60 cm^3 in the X and Z axes. In addition, resolution analysis suggests that the plutonium pit would be located about 30 cm below its true depth location.

Based on the example that is presented and several other models that are analyzed, this threshold E is approximated as

$$E \approx \frac{\rho_{\max}}{\rho_{\mathrm{IQR}(.25)}} \rho_{\mathrm{avg}} \tag{20}$$

where $\rho_{\max}$ is the maximum recovered density; $\rho_{\mathrm{IQR}(.25)}$ is the first quantile [47] of the recovered density, assuming upper and nonnegative bound constraints and a robust estimator of $p = 1$; and ρ_{avg} is the average density of the container. In Fig. 7, (20) estimates a threshold value of $E = 1.05$ g/cm^3. If there are multiple high-density regions, (20) estimates a threshold for only the region with the highest recovered density. Whereas we infer the presence of fissile material, we are not able to quantify how many instances of fissile material are likely.

V. Experimental Validation

A model with increased complexity is shown in Fig. 11 to further experimentally validate the inversion methodology discussed previously. The logarithmic barrier term is again used to constrain the recovered density values, and $p = 1.0$ is used to recover sharp boundaries. This example is different from Fig. 3 in two ways: 1) Increased clutter is added to the container. 2) Non-Gaussian (i.e., uniform) noise is added to the data.

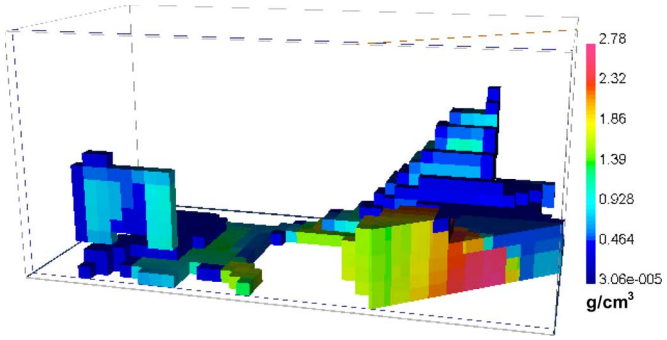

Fig. 12. Recovered model from Fig. 11. This image does not include model cells with density values of less than 2% of the maximum recovered value. This image is also sliced diagonally in the front right for clarity. Comparing this figure with Fig. 11, the plutonium is mostly recovered in the correct location, and the threshold that is calculated by (20) correctly flags the presence of high-density possibly fissile material.

All other parameters between the two models are equal, and because the regularization parameter in (7) was not changed for non-Gaussian noise, the resolution matrices and the funnel analysis are identical.

The recovered image of Fig. 12 does not display model cells with recovered values of less than 2% of the maximum recovered density and is sliced diagonally for clarity. The maximum recovered density of 2.78 g/cm^3 occupies 15 model cells in the same approximate area as the original plutonium's 27 model cells. The threshold of this recovered model from (20) is 1.65 g/cm^3; thus, this container would be flagged for possible presence of fissile material. The effect of noise type on the recovered model is also examined. While Fig. 12 is the result of inverting data corrupted with 2% uniform noise, inversion of the same data corrupted with 2% Gaussian noise produces essentially identical models.

It is clear from Fig. 12 that gravity gradiometry has recovered the area of high density, but the areas of lower density are not well resolved. This is primarily due to the lack of inherent depth resolution in gravity-gradiometry data, regularization, and the p value that is specifically chosen to recover localized high-contrast targets.

VI. Conclusion

The purpose of this research is to examine the feasibility of inferring the presence of fissile materials in a cargo container. Given the total recovered mass of the cargo container from the inversion process, the mass distribution, and the lower and upper bounds of the identified high-density regions, we seek to establish a threshold above which fissile material is likely present. This research attempts to optimize the variance and resolution of the gravity-gradient-imaging problem through the use of robust estimators to recover sharp boundaries and estimations for the variance and resolution of the recovered model, yet there still is a great deal of nonuniqueness that is inherent in the recovered models. It should be noted that, although the choice of p in (5) and the application of log barrier terms were based on problem geometry, recovered models still suffer from such nonuniqueness. Thus, the rationale behind forming the resolution matrix and performing funnel analysis is in direct response to this nonuniqueness: We seek to measure the quality of recovered models using the tools that are developed in this paper.

Funnel analysis provides lower and upper bounds for volumes of recovered bodies. It was shown that the lower bound is less diagnostic than the upper bound. Given a recovered anomaly, the upper bound of funnel analysis can be used to determine if the material has a density that is high enough to be fissile material. Funnel analysis shows that for the plutonium and Uranium synthetic model, there can be no certainty on the recovered density value until the volume exceeds about 125 model cells. Furthermore, the resolution matrix is used to quantify errors in the location of a recovered anomaly. It is noted that recovered anomalies are pushed too deep in the downward Z axis but are centered in the X and Y axes. These results suggest that gravity gradiometry can be successful at identifying suspect high-density areas of cargo containers, but since the volume of fissile materials is expected to be small, any certain determination would require a complementary technique such as neutron detection or manual inspection. It is also important to note that other techniques can be used in place of funnel analysis [34]–[37], [48].

Sensor array optimization and increased sampling density could further decrease the variance and increase resolution. An additional way to increase the resolution is to optimize the α parameters in (5), which are initially set to $\alpha_x = \alpha_y = \alpha_z = 1.0$. Based on the results in the previous section, which found the resolution in the Y dimension that is greater than the resolution in the X dimension, we could modify (5) by increasing α_y with respect to α_x. Furthermore, the previous section found recovered models that are biased in the vertical Z dimension. This artifact can be compensated by decreasing the static component in the cell weighting factors that are discussed in Section III.

Based on the results of this paper, future application of gravity-gradient data toward cargo-container imaging could best be used as a first estimation for recovering densities that are unexpected from the mandatory packing list of every cargo container. It is also worthwhile to consider other additional constraints that are applied to the inversion such as an absolute weight measurement of the cargo container before inversion, a moment of inertia measurement for each of the container axes to constrain the inversion axes, and a maximum trailer density that is calculated from structural integrity limits of Corten steel. Since cargo-container mass is conserved in the recovered models, this value could be used to place an additional upper bounds on the maximum recovered density.

Acknowledgment

The authors would like to thank R. Shekhtman (University of British Colombia) for providing a Huber norm template and J. Berryman (Lawrence Berkeley National Laboratory) for useful discussions on robust estimators. They would also like to thank M. Talwani, three anonymous reviewers, and the Associate Editor for their helpful suggestions that have significantly improved this paper.

REFERENCES

[1] R. E. Bell, "Gravity gradiometry," *Sci. Amer.*, vol. 278, no. 6, pp. 74–80, 1998.

[2] J. Kusche and R. Klees, "Regularization of gravity field estimation from satellite gravity gradients," *J. Geod.*, vol. 76, no. 6/7, pp. 359–368, 2002.

[3] D. W. Vasco and C. Taylor, "Inversion of airborne gravity gradiometry data, southwestern Oklahoma," *Geophysics*, vol. 56, no. 1, pp. 90–101, 1991.

[4] R. E. Bell, L. F. Pratson, R. Anderson, and E. K. Biegert, "Gravity gradiometry; applications to basin analysis," *Trans. Amer. Geophys. Union*, vol. 76, no. 46, p. 143, 1995. AGU 1995 fall meeting, Eos, Suppl.

[5] L. F. Pratson, R. Bell, R. Anderson, D. Dosch, J. White, C. Affleck, A. Grierson, B. Korn, R. Phair, E. Biegert, and P. Gale, "Results from a high-resolution, 3-D marine gravity gradiometry survey over a buried salt structure," *Trans. Amer. Geophys. Union*, vol. 76, no. 46, p. 144, 1995. Mississippi Canyon area, Gulf of Mexico, AGU 1995 fall meeting, Eos, Suppl.

[6] M. H. Dransfield and J. B. Lee, "The Falcon airborne gravity gradiometer survey system," in *Proc. Australian Soc. Exploration Geophys.-PESA Airborne Gravity Workshop*, Sydney, Australia, 2004, pp. 15–20.

[7] A. G. Nekut, "Borehole gravity gradiometry," *Geophysics*, vol. 54, no. 2, pp. 225–334, 1989.

[8] B. A. Kirkendall, J. P. Lewis, and P. E. Harben, "Advances of crosswell electromagnetics in steel casing," in *Proc. Soc. Exploration Geophys. Annu. Meeting, Extended Abstracts*, Dallas, TX, 1999, pp. 323–326.

[9] B. Kirkendall, Y. Li, and D. Oldenburg, "Imaging cargo containers using gravity gradiometry," in *Proc. SPIE Defense and Security Symp.*, Kissimmee, FL, Apr. 16–20, 2006. v. 6204. [Online]. Available: www.spie.org

[10] G. M. Hofmeyer and C. A. Affleck, "Rotating accelerometer gradiometer," U.S. Patent 5 357 802, Oct. 25, 1994. [Online]. Available: www.uspto.gov

[11] GEDEX, Mississauga, ON, Canada. [Online]. Available: http://www.gedex.ca/

[12] A. N. Tikhonov and V. Y. Arsenin, *Solutions of Ill Posed Problems*. New York: Wiley, 1977.

[13] F. J. Anscombe, "Rejection of outliers," *Technometrics*, vol. 2, no. 2, pp. 123–147, May 1960.

[14] Y. Li and D. W. Oldenburg, "3-D inversion of gravity data," *Geophysics*, vol. 63, no. 1, pp. 109–119, 1998.

[15] Y. Li and D. W. Oldenburg, "Fast inversion of large-scale magnetic data using wavelet transforms and a logarithmic barrier method," *Geophys. J. Int.*, vol. 152, no. 2, pp. 251–265, Jan. 2003.

[16] Y. Li and D. W. Oldenburg, "Joint inversion of surface and three-component borehole magnetic data," *Geophysics*, vol. 65, no. 2, pp. 540–552, 2000.

[17] Y. Li, "3D Inversion of gravity gradiometry data," in *Proc. Soc. Explor. Geophys. Annu. Meeting Expanded Abstracts*, 2001.

[18] Y. Li and D. W. Oldenburg, "3-D Inversion of magnetic data," *Geophysics*, vol. 61, no. 2, pp. 394–408, 1996.

[19] C. G. Farquharson and D. W. Oldenburg, "Non-linear inversion using general measures of data misfit and model structure," *R. Astron. Soc. Geophys. J. Int.*, vol. 134, no. 1, pp. 213–227, 1998.

[20] E. Haber, "Numerical strategies for the solution of inverse problems," Ph.D. dissertation, Univ. British Columbia, Vancouver, BC, Canada, 1996.

[21] J. R. Shewchuk, *An Introduction to the Conjugate Gradient Method Without the Agonizing Pain*, 1.25 ed. Pittsburg, PA: School Comput. Sci., Carnegie Mellon, 1994.

[22] D. W. Oldenburg and Y. Li, "Subspace linear inverse method," *Inverse Theory*, vol. 10, no. 4, pp. 915–935, Aug. 1994.

[23] S. J. Wright, *Primal-Dual Interior Point Methods*. Philadelphia, PA: Soc. Ind. and Appl. Math., 1997.

[24] G. B. Dantzig, *Linear Programming and Extensions*. Princeton, NJ: Princeton Univ. Press, 1963.

[25] J. Nocedal and S. J. Wright, *Numerical Optimization*. New York: Springer-Verlag, 1999.

[26] O. Portniaguine and M. S. Zhdanov, "Focusing geophysical inversion images," *Geophysics*, vol. 64, no. 3, pp. 874–887, 1999.

[27] K. W. Bowyer and N. Ahuja, *Advances in Image Understanding: A Festschrift for Azriel Rosenfeld*. Hoboken, NJ: Wiley, 1996. 358 pp.

[28] P. J. Huber, *Robust Statistical Procedures*, 2nd ed. Philadelphia, PA: SIAM, 1996. 68, 67 pp.

[29] J. A. Scales and A. Gersztenkorn, "Robust methods in inverse theory," *Inverse Probl.*, vol. 4, no. 4, pp. 1071–1091, 1998.

[30] J. A. Scales, A. Gersztenkorn, and S. Treitel, "Fast LP solution of large, sparse, linear systems: Application to seismic travel time tomography," *J. Comput. Phys.*, vol. 75, pp. 314–333, 1998.

[31] C. F. Gauss, "Theoria motus corporum coelestium in sectionibus conicis solem ambientium," *Giornale di Astronomia*, vol. 27, no. 1, pp. 24–31, 2001, Hamburg, Germany. (Original English Trans. Charles Henry Davis, Little, Brown, and Company, Boston, 1857), 1809 orig.

[32] W. Li and J. J. Swetits, "The linear L_1 estimator and the Huber M-estimator," *SIAM J. Optim.*, vol. 8, no. 2, pp. 457–475, 1998.

[33] R. Snieder, "The role of nonlinearity in inverse problems," *Inverse Probl.*, vol. 14, no. 3, pp. 387–404, Jun. 1998.

[34] M. Sambridge, C. Beghein, F. Simons, and R. Snieder, "How do we understand and visualize uncertainty?" *Lead. Edge*, vol. 25, no. 5, pp. 542–546, May 2006.

[35] D. W. Vasco, "Resolution and variance operators of gravity and gravity gradiometry," *Geophysics*, vol. 54, no. 7, pp. 889–899, 1989.

[36] A. Hero and J. A. Fessler, "A recursive algorithm for computing Cramer–Rao-type bounds on estimator covariance," *IEEE Trans. Inf. Theory*, vol. 40, no. 4, pp. 1205–1210, Jul. 1994.

[37] H. L. Van Trees, *Detection, Estimation, and Modulation Theory*. Hoboken, NJ: Wiley, 2001. 720 p.

[38] D. W. Oldenburg, "Funnel functions in linear and nonlinear appraisal," *J. Geophys. Res.*, vol. 88, no. B9, pp. 7387–7398, 1983.

[39] D. Oldenburg and Y. Li, "Geophysical inversion, A tutorial," *Near-surface geophysics: Soc. Explor. Geophys. Investigations Geophys.*, D. K. Butler, Ed., vol. 13, no. 13, pp. 89–150, 2005.

[40] J. H. Wilkinson, *Rounding Errors in Algebraic Processes*. New York: Courier Dover Publications, 1994. 161 pp.

[41] D. L. Alumbaugh and G. A. Newman, "Image appraisal for 2-D and 3-D electromagnetic inversion," *Geophysics*, vol. 65, no. 5, pp. 1455–1467, 2000.

[42] D. L. Alumbaugh, "Linearized and nonlinear parameter variance estimation for two-dimensional electromagnetic induction inversion," *Inverse Probl.*, vol. 16, no. 5, pp. 1323–1341, Oct. 2000.

[43] P. S. Routh, G. A. Oldenborger, and D. W. Oldenburg, "Optimal survey design using the point spread function measure of resolution," in *Proc. Soc. Explor. Geophys. Annu. Meeting Expanded Abstracts*, 2005, vol. 24, p. 1033.

[44] R. Parker, *Geophysical Inverse Theory*. Princeton, NJ: Princeton Univ. Press, 1994. 400 pp.

[45] M. Greenacre, *Multiple Correspondence Analysis and Related Methods*. London, U.K.: Chapman & Hall, 2006. 608 p.

[46] W. Menke, *Geophysical Data Analysis: Discrete Inverse Theory*, vol. 45. New York: Academic, 1989. International Geophysical Series, 289 pp.

[47] S. B. Vardeman and J. M. Jobe, *Basic Engineering Data Collection and Analysis*. Pacific Grove, CA: Duxbury Thomson Learning, 2001. 832 pp.

[48] P. J. Stephens and A. S. Jones, "Bounds on the variance in the pattern matching criteria," *IEEE Trans. Geosci. Remote Sens.*, vol. 9, no. 9, pp. 2514–2522, Sep. 2006.

Barry Kirkendall received the B.Sc. degree in physics from the University of California, San Diego, in 1992 and the M.Sc. degree in geophysics from Colorado School of Mines, Golden, in 1998. He is currently working toward the Ph.D. degree at Colorado School of Mines.

He began his research career in marine seismology at Scripps Institution of Oceanography, La Jolla, CA. He was later an Electrical Engineer at Caterpillar Inc. and has been a Physicist at Lawrence Livermore National Laboratory, Livermore, CA, since 1998. His research interests are focused on diffusive and propagation electromagnetic modeling, gravity and magnetic modeling, inverse theory, and instrumentation and data acquisition.

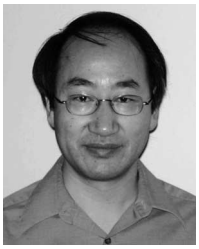

Yaoguo Li received the B.A.Sc. degree in geophysics from Wuhan College of Geology, Wuhan, China, in 1983 and the Ph.D. degree in geophysics from the University of British Columbia (UBC), Vancouver, BC, Canada, in 1992.

He was with the UBC-Geophysical Inversion Facility, UBC, from 1992 to 1999, first as a Postdoctoral Fellow and then as a Research Associate. He is currently an Associate Professor of geophysics in the Department of Geophysics, Colorado School of Mines, Golden, where he directs the Center for Gravity, Electrical, and Magnetic Studies, which carries out research on exploration geophysics that is sponsored by petroleum and mining industries and on UXO detection and discrimination that is funded by SERDP and USACE. His research interests include geophysical inverse theory; inversion of gravity, magnetic, and electromagnetic data arising from applied geophysics; and their application to environmental and resource-exploration problems.

Prof. Li was a corecipient of the 1999 Gerald W. Hohmann Award. He is a Member of the American Geophysical Union, Environmental and Engineering Society, and Society of Exploration Geophysicists.

Douglas Oldenburg received the B.Sc. degree (Honors) in physics and the M.Sc. degree in geophysics from the University of Alberta, Edmonton, AB, Canada, and the Ph.D. degree in earth sciences from the University of California, San Diego, in 1974.

After a three-year postdoc, he joined the Department of Earth and Ocean Sciences, University of British Columbia, Vancouver, BC, Canada, where he is currently a Professor, the Director of the Geophysical Inversion Facility, and the holder of the TeckCominco Senior Keevil Chair in Mineral Exploration.